Available online at www.sciencedirect.com

jmr&t Journal of Materials Research and Technology

journal homepage: www.elsevier.com/locate/jmrt

Miniaturised experimental simulation of open-die forging

David Connolly [a,b,*], *Giribaskar Sivaswamy* [a], *Salaheddin Rahimi* [a], *Vassili Vorontsov* [b]

[a] *Advanced Forming Research Centre (AFRC), University of Strathclyde, Inchinnan, Renfrewshire PA4 9LJ, UK*
[b] *Design Manufacture and Engineering Management (DMEM), University of Strathclyde, Glasgow G1 1XJ, UK*

ARTICLE INFO

Article history:
Received 30 May 2023
Accepted 8 August 2023

Keywords:
Open-die forging
Equipment design
Materials processing
Cogging
Process modelling

ABSTRACT

This study presents a novel experimental set-up for laboratory-scale simulation of cogging and open-die forging processes during ingot-to-billet conversion of advanced engineering alloys. The experimental set-up is designed to be cost-effective, employing a remotely operated manipulator assembly constructed from readily available "off-the-shelf" components used in conjunction with a conventional uni-axial load-frame - equipment that is available in most materials testing laboratories. Small test-bars of C101 copper alloy were subjected to multi-stroke cogging operations with intermittent rotation at ambient and elevated temperatures (20–600 °C). Prior to forging, the as-received material underwent heat treatments to coarsen the starting grain structure, and to help demonstrate the capability of the apparatus to achieve grain refinement via recrystallisation (dynamic and static) and recovery processes within the deformed material. The resulting microstructural evolution and mechanical property changes of the forged material have been investigated using light microscopy (LM), Vickers hardness (HV) testing, and electron backscatter diffraction (EBSD). The deformed C101 alloy exhibited measurable grain refinement after forging at elevated temperatures, thus demonstrating the effectiveness of the designed miniaturised open-die forging set-up.

1. Introduction

Precise control of microstructure evolution is of paramount importance during all metallurgical manufacturing processes, and is essential for achieving optimal mechanical properties in the final manufactured components. Thermomechanical processing used for ingot-to-billet conversion of high-performance alloys is no exception. The high-temperature plastic deformation must be sufficient to promote complete recrystallisation of the coarse-grained as-cast ingot structure into a final billet with refined grains. The success of this process is fundamental in the production of high-value metallurgical components, since any inhomogeneities in the resulting microstructure are inherited during all subsequent processing steps (*e.g.*, closed-die forging) and are ultimately carried forward into the final product. Therefore, understanding the phenomenology of microstructural transformations during the ingot-to-billet conversion stage is key for the overall manufacturing route.

* Corresponding author. 85 Inchinnan Dr, Inchinnan, Renfrew, Scotland, UK.
E-mail address: david.connolly@strath.ac.uk (D. Connolly).
https://doi.org/10.1016/j.jmrt.2023.08.073

Grain size control via thermomechanical processing is a very effective way of attaining improved mechanical properties. This change in grain size, is significantly linked with dynamic, metadynamic, and static recrystallisation during hot deformation. Recrystallisation kinetics are very complex and are greatly influenced by process variables, such as the forging temperature, strain rate, initial grain size, and the level of plastic deformation, which have been studied through analysis of Inconel®-718 alloy by Yeom et al. [1], and nickel superalloy AD730® by Coyne-Grell et al. [2,3] To predict the grain-size distribution in finished components, the development of microstructure evolution models has received considerable attention in recent years, *e.g.,* numerical models studies of cogging by Kukuryk et al. [4], 3D thermo-viscoplastic finite element analysis by Cho et al. [5] and recrystallisation modelling of superalloys by Dong et al. [6].

Process modelling has remained the forefront of research in this area as the conventional ingot-to-billet conversion cogging process is an expensive, resource-intensive, and complex procedure, which is evidenced throughout the works of Perez et al. [7] and Souza et al. [8,9] Laboratory tests following the ASTM E209-18 [10] standard have only ever captured kinetics for the upsetting process. However, this leaves a considerable gap in knowledge of the other main ingot-to-billet process at this scale - cogging. Thus, developing a cost-effective, reproducible method for exploring the various mechanisms of cogging, may not only lead to savings in energy, material, time, and capital investment, but would be an effective tool for future experimental research.

This work proposes the design elements of a novel laboratory-scale cogging method, discusses the observed challenges of the design and proof-of-concept experiments, and makes recommendations for future improvements. The approach offers a cost-effective experimental methodology that could be employed in conjunction with computer simulations, before committing to more costly forging trials at larger scales. An understanding of the size effects regarding billet geometries, plastic strain levels, grain refinement, and microstructural evolution is vital to the successful application of reduced-scale experimental methods. With large investment in experimentation at "close-to-industry scale" such as the ATI[1] funded Future Forge project, evidenced in the works of Ward et al. [11], Rahimi et al. [12] and Blackwell et al. [13], it is crucial to ensure the equivalence and relevance/applicability to the industrially manufactured material. Identifying such length scale trends is fertile ground for numerous stand-alone investigations involving matrix tests over the relevant process parameter variable ranges, followed by extensive microstructural characterization. For brevity, we limit the present discussion to the evaluation of the devised experimental methodology in its overall ability to attain measurable control over the grain–refinement processes. More detailed investigations on single-phase and dual-phase alloys will be described elsewhere.

[1] *Aerospace Technology Institute (ATI), creates the technology strategy for the UK aerospace sector and funds world-class research and development.*

2. Experimental equipment design

The experimental apparatus design relies on the use of the extensometer slot in laboratory-scale furnaces typically used for thermomechanical testing on uni-axial load frames. For furnaces, where such a slot is not available, the apparatus may still be used, *e.g.,* by using a partly open split-tube furnace with clamps loosened and gaps filled with ceramic wool. This section will detail the main elements of the equipment design and discuss some of the key design considerations of each. The overall apparatus design employs an assembly of commercially available components and a limited number of custom-manufactured parts.

2.1. *Motion actuator sub-assembly*

The motion actuator sub-assembly (seen in Fig. 1) is designed around an off-the-shelf pre-assembled linear motion mechanism. The mechanism uses a profiled aluminium extrusion as its frame, which supports a 12 mm wide linear guide-way along its length. A CNC-machined aluminium platform is mounted to the guide-way carriage and is able to slide from one end of the guide-way to the other. A 500 mm long 12 mm diameter lead screw runs through a matched nut in the platform and spans the entire length of the frame. Two Nanotec® ST4118L NEMA17 stepper motors (with 200 steps per revolution) actuate the motions of the apparatus during specimen testing and positioning. One of the motors is mechanically coupled with the lead screw and is used for lateral translation of the aluminium platform. This lateral movement allows both the entry and removal of the test specimens from the furnace, as well as adjustment of their position within the mechanical working zone (*i.e.,* their location relative to the compression dies). The second motor is mounted using a standard L-bracket to the lead screw platform. This motor is used for the axial rotation of the specimen manipulator assembly via a cylindrical coupling. In addition to providing controlled rotation of the workpiece between compression bites, the motor additionally applies a holding torque during compression to aid against workpiece slippage.

Two custom components have been added to the actuator assembly. Firstly, a mount, consisting of stacked ABS plates connected to a Manfrotto™ quick-release camera tripod mount, is attached with screws to the base extrusion of the linear motion mechanism. This allows the attachment of the motion actuator assembly to a heavy-duty adjustable camera tripod, allowing for height, pitch, yaw, and roll adjustments into the relevant positioning for the furnace and load frame. Adapting the actuator for mounting to a tripod allowed for considerable portability and freedom of adjustment without requiring any modifications to be made to the load frame. However, improvements to this design will be explored in the discussion.

The second component is an extendable specimen manipulator support, machined from 316 stainless steel sheets. It is connected with screws to the sides of the motion actuator frame via square nuts in the guide slots in the extrusion. The main function of this extendable support is the horizontal support of the specimen manipulator rod in the

vicinity of the furnace door. This addition aids against excessive vertical and horizontal deflection of the manipulator rod during testing. Fig. 1 shows a detailed representation of the experimental arrangement of components and specimen placement within the tube furnace interior.

2.2. *Electronic controller*

The electronic controller unit was constructed around an Arduino® MEGA 2560 R3 microcontroller development board coupled with a KEYESTUDIO™ MEGA sensor shield V1 to facilitate the connection of the required module boards. The controller firmware was programmed and compiled using the popular free-and-open-source Arduino® IDE software which uses the C++ language. A 24 V 6.25 A AC-DC switching mode power supply was used to power stepper motors of the motion actuator assembly, while an LM2596 DC–DC buck converter module was used to step-down the voltage to 5 V to safely power to the microcontroller board connected associated modules. Two motor driver modules based on the DRV8825 chip were used to control the primary and secondary stepper motors. Two 4N25 optocouplers were used for isolation of

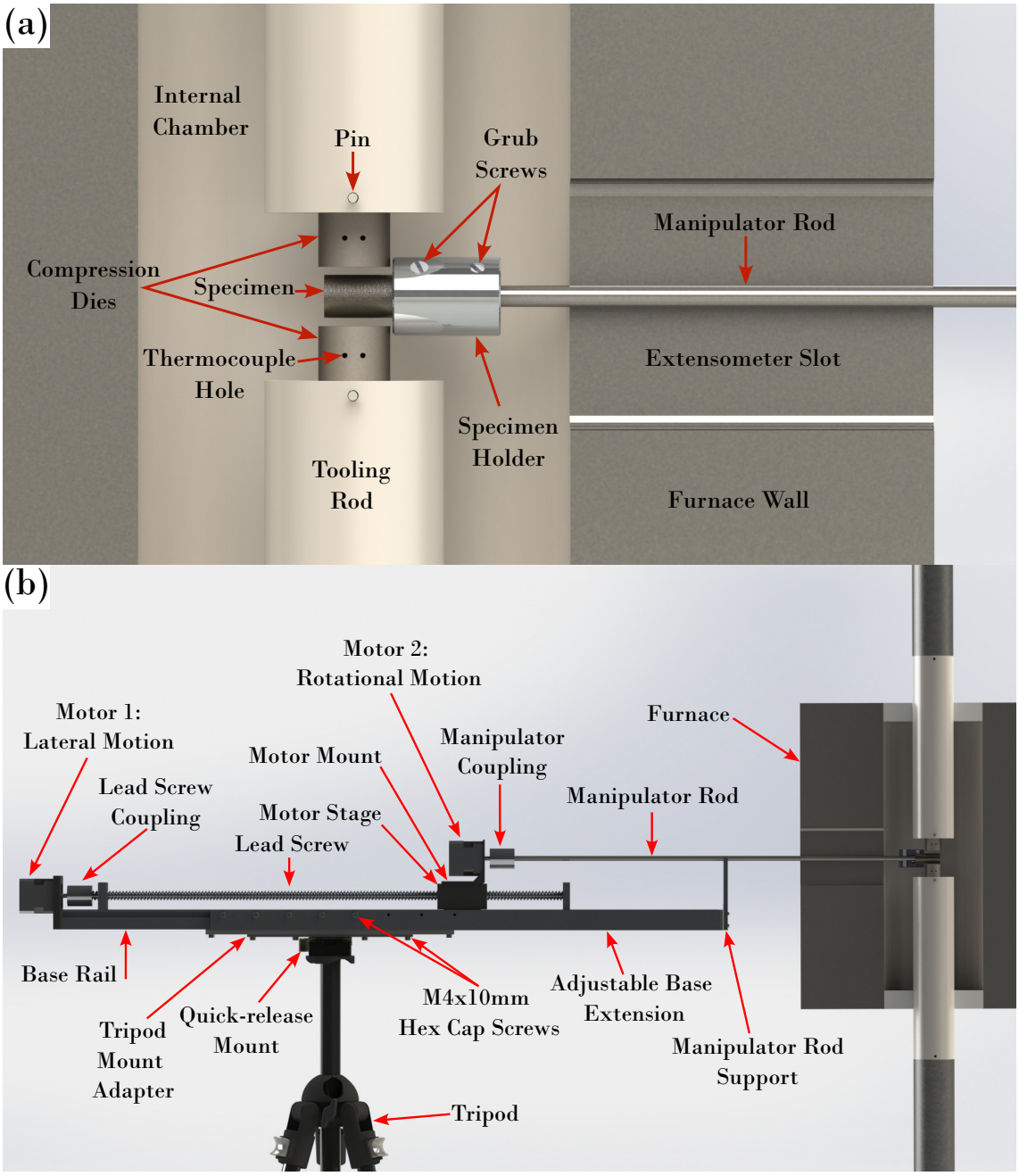

Fig. 1 – (a) CAD rendering of the internal furnace chamber during test set-up, showing the arrangement of the workpiece, dies, and manipulator, (b) CAD rendering showing a side profile of the component arrangement in the experimental set-up. Both were generated using Dassault Systémes SOLIDWORKS®, rendered with Photoview 360.

input and output electrical signals between the controller of the Zwick/Roell™ load frame, with standard BNC male connectors provided for the use of shielded coaxial cables. A standard ABS instrument enclosure was used to house the electronic components, with the front and rear panels laser-cut to allow the mounting of an LCD screen, user interface buttons, and other switches and connectors. The operator controls and interface are shown in Fig. 2(a), while a schematic of the electrical connections used in the electronic controller assembly can be seen in the supplementary material.

2.3. *Tooling*

Two pairs of custom-manufactured platens were used as compression die sets: one used for ambient temperature and the other for elevated temperature testing. The cylindrical platens, 20 mm in diameter, 15 mm in height, were manufactured by wire electric discharge machining (EDM) from IN718 and Nimonic®-90 nickel-base superalloys, respectively. The platen size was determined by the internal volume available within the vertical split-tube furnace used for the highest temperature experiments. The inner diameter of the furnace was 80 mm, and the platens needed to allow enough room for the specimen grip at the end of the manipulator rod. This also permitted placement of the specimens over the entire span of the dies to avoid equipment damage due to uneven loading.

Sets of manipulator rods 8 mm in diameter were manufactured to allow testing over a range of temperatures. Accompanying sets of standard cylindrical couplings with a range of internal diameters were also procured for the purpose of motion transmission from the rotation-axis stepper-motor to the manipulator rods and, hence, the specimens. The manipulator rods were manufactured from type.

Sets of cylindrical couplings were manufactured and mounted on the opposing ends of the manipulator rods for gripping of the test specimens during the positioning and

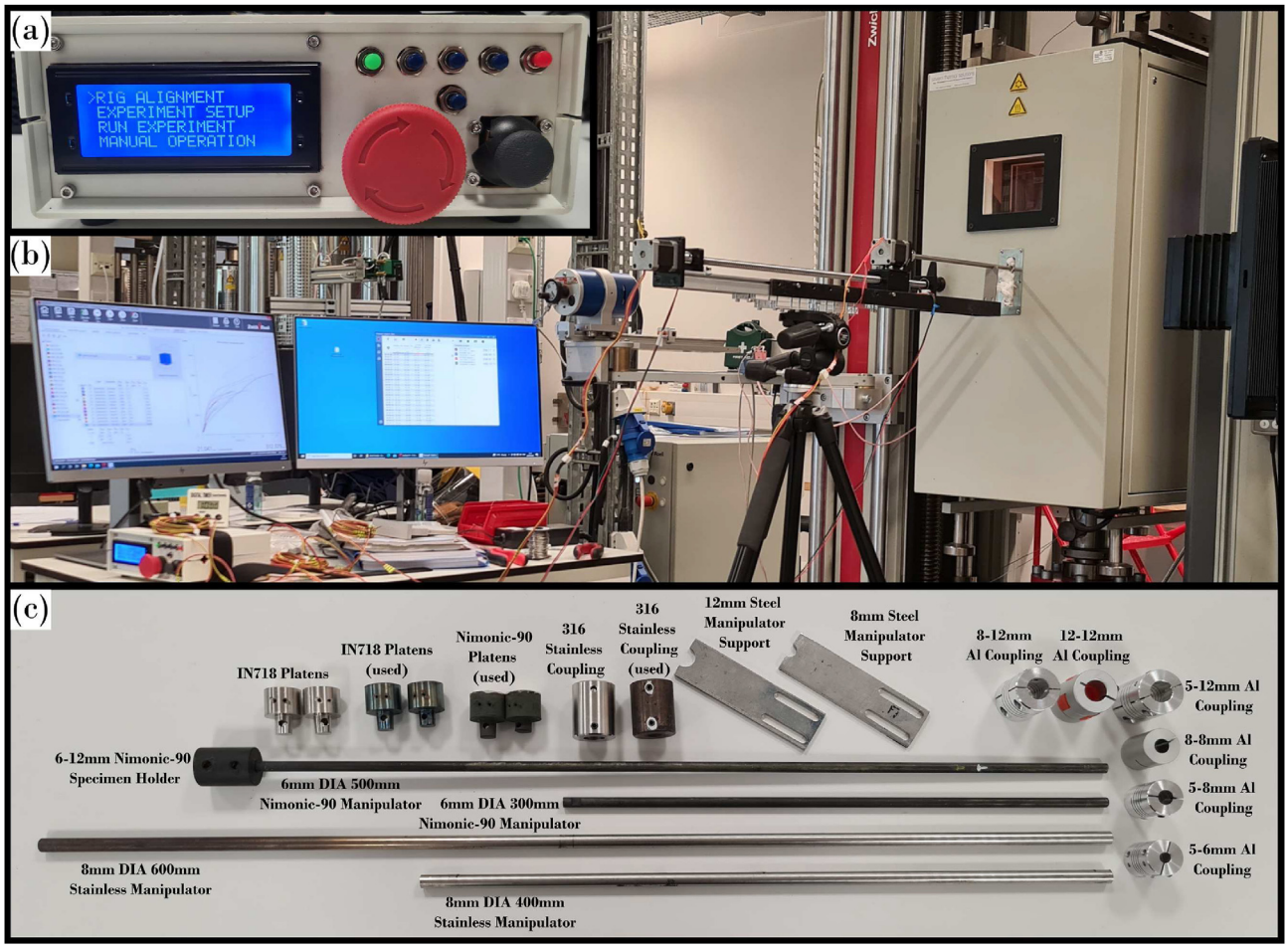

Fig. 2 – Collection of experimental operation, set-up and tooling showing: (a) an image of the front operator interface of the control box, (b) an image of full laboratory set-up during testing, showing arrangement of design methodology within Zwick/Roell™ load frame and utilisation of the Severn Thermal Solutions EC2112 environmental chamber and use of ceramic wool for thermal insulation. Also showing the use of the Electronic Controller, in conjunction with the Zwick™ testXpert III software, (c) an image showing the collection of experimental tooling, including experimental platens, manipulator rods, manipulator rod supports, motor and specimen couplings. 316 stainless steel and Nimonic®-90 superalloy.

forging operations. These 8 mm–12 mm diameter cylinders were cut from type 316 stainless steel and Nimonic®-90 superalloy using wire EDM. All couplings were manufactured with threaded side holes to allow the use of fixating grub screws for both the manipulator rods and the test specimens. Grub screws for high temperature testing were machined from Nimonic®-90.

The elevated temperature testing in this study was carried out at 600 °C and, to extend the longevity of the IN718 platens, boron nitride suspension was used as a lubricant and anti-stick agent. An image showing the full tooling set is shown in Fig. 2(c).

3. Materials and methods

3.1. Material and open-die forging

C101 copper alloy was used as the test specimen material for the pilot forging trials on the designed apparatus. The nominal chemical composition of the material is provided in Table 1. The alloy was procured as 12 mm diameter extruded round bar. Sections of the alloy bar were then subjected to an abnormal grain growth heat treatment in a VFE TAV TPHF horizontal vacuum furnace for 2 h at 800 °C and then air-cooled. This material will henceforth be referred to as "as-heat-treated" (AHT). The AHT bar sections were subsequently cut into shorter test specimens 30–35 mm long, an example of which can be seen in Fig. 3(a).

The open-die forging was carried out on a 250 kN Zwick/Roell™ Amsler Z250 load frame equipped with a Severn Thermal Solutions EC2112 environmental chamber (EC), using the Zwick™ testXpert III software. Initial testing was performed at ambient temperature without the EC and used the standard strain control method. Specimens for elevated temperature testing were first mounted onto the manipulators and then backed through the EC extensometer slot before attachment to the motor coupling. Specimen positioning was then adjusted remotely inside the EC prior to heating and the remaining gaps in the extensometer slot were filled with ceramic wool for thermal insulation. The elevated temperature tests used a step control program method within the textXpert III software. The specimens were then brought to 600 °C and "soaked" for 10 min to ensure a homogeneous and stable temperature distribution. A pre-load of 20 N was applied at the end of the soak time, to aid against specimen slipping. The specimens were then repeatedly deformed in 5% cross-section height reduction increments using a controlled step program. Between each deformation, or "bite", the specimen was rotated 90° (except where specified otherwise) to simulate the cogging (*i.e.*, open-die forging) operation. The manipulator rods were marked at 0° in vision of the operator to track specimen rotation between bites. The test matrix for all the cogging operations conducted on the C101 specimens can be seen in Table 2.

The final cogged geometry target for specimen SP6 was for a reduction of 30% in cross-section height, corresponding to a macroscopic true strain (ε_m) of 0.36, under a nominal strain rate of $0.01s^{-1}$ ($\dot{\varepsilon_m}$). The specimen was then withdrawn from the environmental chamber and allowed to air cool. A schematic diagram of the thermomechanical procedure for the forging test is shown in Fig. 3.

After forging, 3D GOM scans of the samples were captured using the GOM ATOS TripleScan III rotary table scanner. This 3D data was loaded into the GOM Suite and average strains were measured for each sample using section areas taken every 1 mm along the sample. The average strain reduction was then calculated from the difference in area between sections in the stub zone against the cogged zone; these zones are shown in Fig. 4(a).

3.2. Finite element analysis

A 3D finite element method (FEM) simulation of the cogging tests, including the initial heating and soaking stages, was performed using the DEFORM™ software to predict the strain distribution at different locations along the samples, seen in Fig. 5(c) and (d) and Fig. 9. Material data for the respective forging temperatures and strain rates was captured in the lab through standard compression testing, this data was then applied to the FE model. For validation, the flow stress was calculated using the 0.2% proof stress method and was found to be a close match to the flow stress data available within DEFORM™ and published works [14].

A thermal conductivity of 391.1 $W\,m^{-1}\,K$ for C101 was used for heating operations for the workpiece, with a convection coefficient of 0.02 $Ns^{-1}\,mm^{-1}\,C^{-1}$. For the deformation operations, a friction coefficient of 0.3 between the dies and the sample were implemented, as per the software's suggested values for lubricated warm forging. Additionally, the deformation conditions were set up with no heat transfer with the environment, die, and workpiece temperature fixed at 600 °C. A Taylor-Quinney factor of 0.9 was used [15,16], which is a good approximation of the fraction of mechanical work converted into heat during deformation [17–19]. A mesh with 16,000 tetrahedral elements was generated for the workpiece geometry, presented in Fig. 6, with the simulation dies shown in Fig. 6(d). The movement speed of the lower die during the experimental compression tests was recorded, and the measured value was used as an input for the FEM simulation.

The specimen dimensions predicted by the model were compared with the actual dimensions of the deformed specimens after compression. The model was set up to replicate the same compression levels of the various samples up to a macroscopic true strain (ε_m) of 0.7. Fig. 5(c) and (d), provide images that are taken before and after the final 2 simulation

Table 1 – Nominal chemical composition of the C101 copper alloy.

Element	Cu	Pb	Zn	Fe	P	Ag	As	O	Sb	Te
Weight %	Bal.	0.0005	0.0001	0.0010	0.0003	0.0025	0.0005	0.0005	0.0004	0.0002

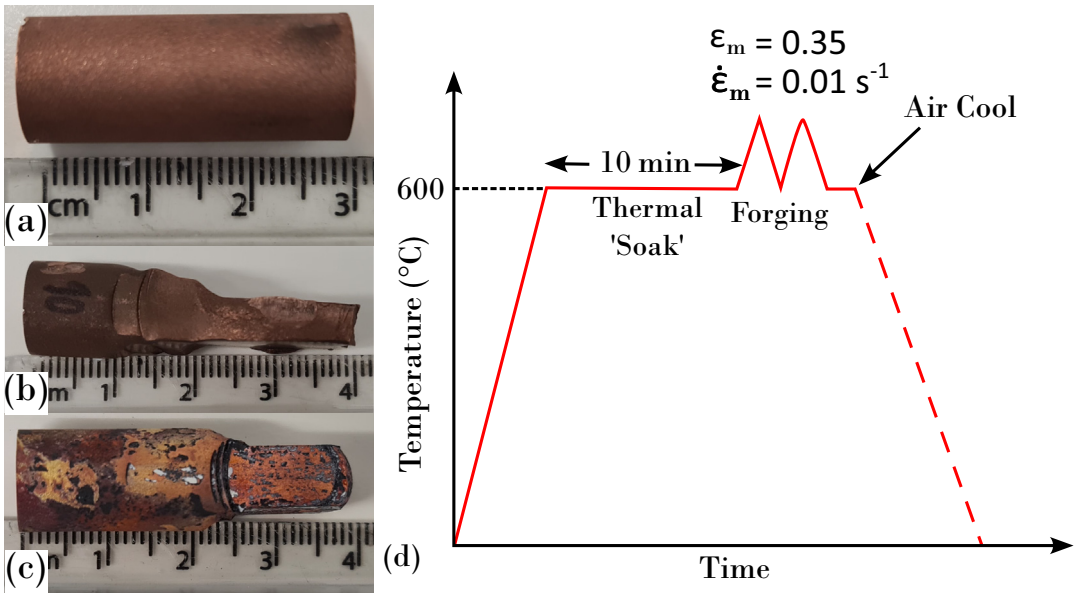

Fig. 3 – (a) Specimen before testing, (b)Benchmark specimen SP1 forged at ambient temperature, (c) Specimen SP6 forged at elevated temperature and, (d) Schematic overview of the elevated temperature compression used in this study.

Table 2 – Test matrix for C101 copper alloy, deformed at ambient and elevated temperatures, detailing number of bites, % of deformation (reduction in cross-sectional height), and specimen geometry targets.

Specimen No.	SP1	SP2	SP3	SP4	SP5	SP6	SP7	SP8
Target Reduction in Cross-section (%)	30(Control)	5	10	15	15	30	40	10
Target Geometry	Square	Square	Square	Square	Square	Square	Square (2 Passes)	Octagonal
Total No. of Bites	12	2	4	6	6	12	16	8
Temperature (°C)	20	20	20	20	600	600	600	600

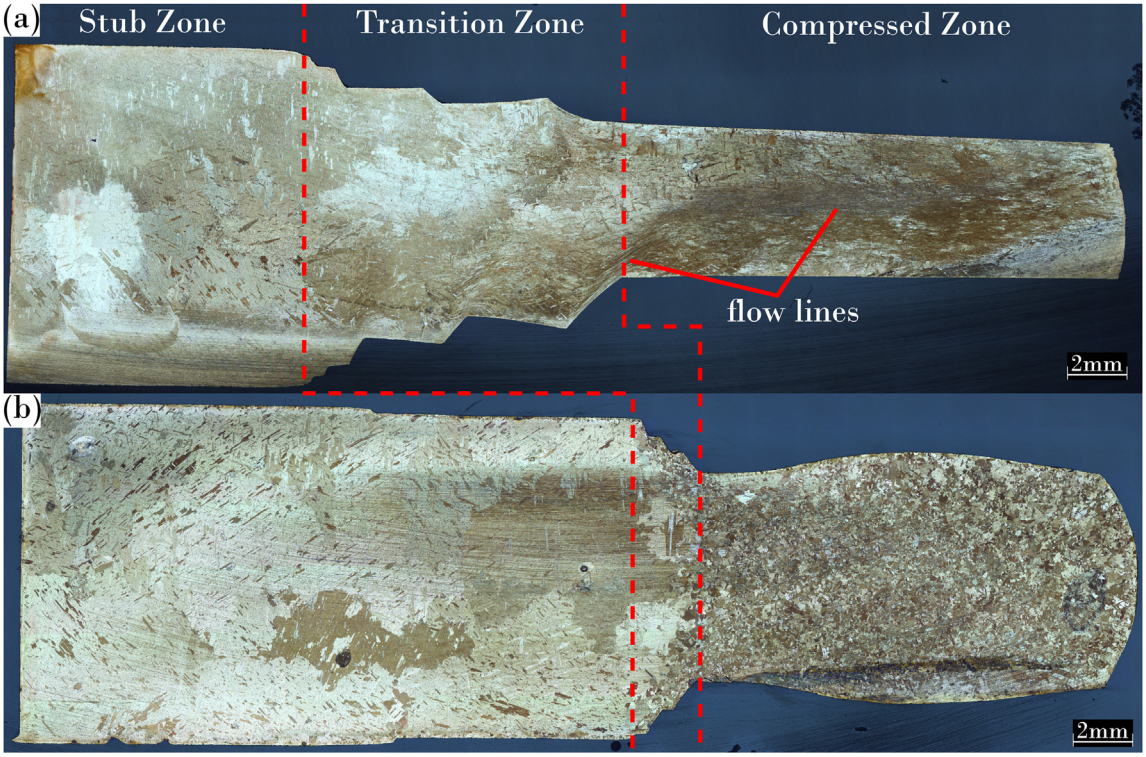

Fig. 4 – Macrographs of the C101 specimens following cogging trials (a) SP1, (b) SP6, both after a 30% nominal reduction in area after cogging), highlighting Stub, Transition, and Cogged zones in both specimens.

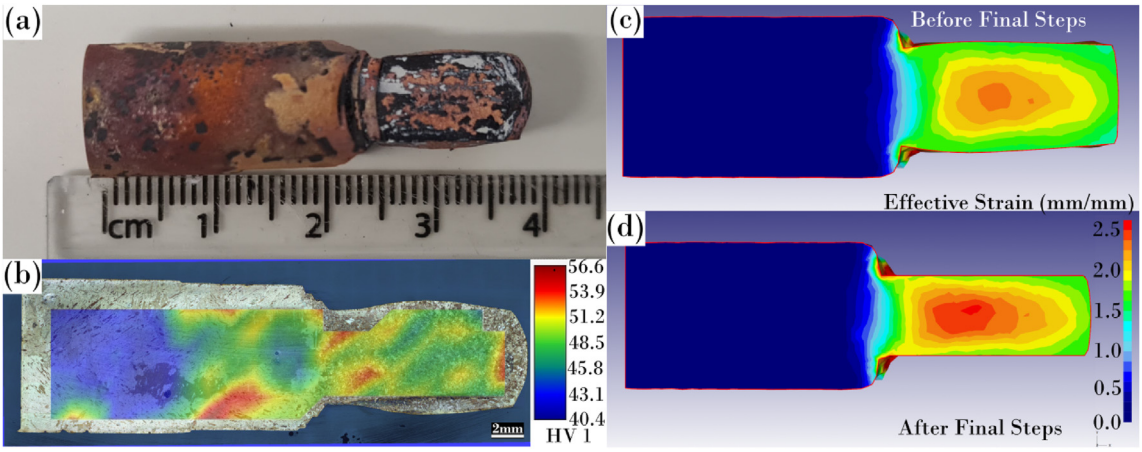

Fig. 5 – (a) A photograph of specimen SP6 image after the cogging trial, (b) An optical micrograph of the cross-section of specimen SP6 with overlaid microhardness, (c) + (d) the result of the FE simulation of the open-die forging of specimen SP6 to an area reduction within 1.5%, (c) prior to final simulation step straightening and, (d) after final simulation step straightening, both using the same effective strain scalebar, acquired using DEFORM™ software.

steps for the last 45% cross-section reduction bite respectively, this figure demonstrates that the final 2 steps straighten the billet in the model, yet are of approximately the same effective strain level. The FE models match the geometry of the deformed parts, and predicts a maximum final average cross-section height of 6.37 mm, which was within 2% of the measured average cross-section height of 6.25 mm. This validates the chosen values of heat transfer coefficient and friction coefficient, and suggests that the strain distribution is reasonably accurate.

3.3. *Microstructure characterization*

The deformed samples were sectioned along the longitudinal axis using EDM, cold-mounted in non-conductive epoxy resin, ground using silicon carbide abrasive papers and polished

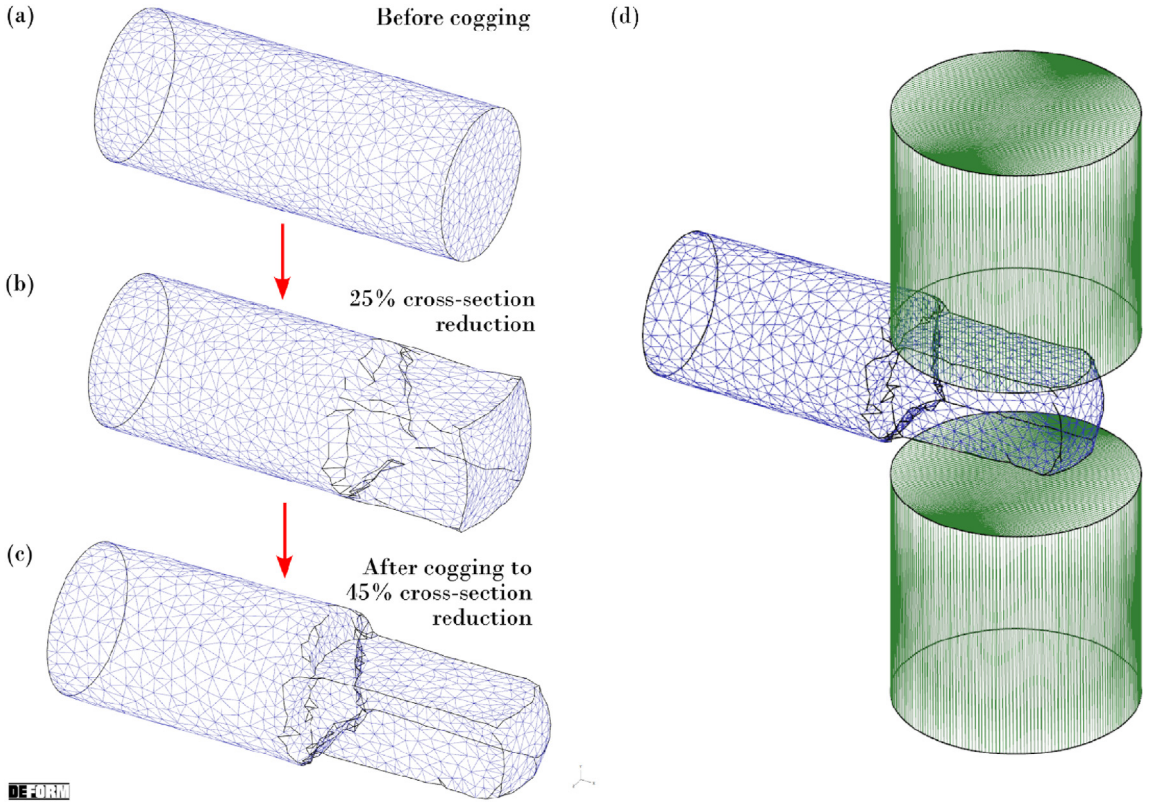

Fig. 6 – (a) The FE generated mesh for specimen SP6 following cogging trial, showing the mesh (a) before cogging, (b) during cogging at 25% cross-section reduction, (c) after cogging to 45% cross-section reduction and, (d) before second cogging bite at 45% cross-section reduction with cogging dies shown.

with colloidal silica suspension to a mirror finished condition. The specimens were subjected to a final etching by immersion of approximately 15–25 s per sample. The etching reagent used was a solution of 4–6 ml nitric acid in 9 ml water. This water-to-acid proportion was selected because a 1:1 ratio proved too aggressive. Light micrographs were then acquired using a Leica™ DM12000 microscope with a motorised stage. First, an overall macro image of the entire sample was taken, and then higher resolution micrographs were acquired in 3 zones, including stub, transition, and cogged zones; these zones are highlighted in Fig. 4(a). The mean linear intercept method was used within ImageJ software to determine average grain size in the stub and cogged zones, which were then used to calculate the reduction in grain size.

The specimens were also hot-mounted in conductive bakelite and ground and polished to a mirror finish, before subjecting to a final vibratory polishing for 1 h using 0.02 μm colloidal silica suspension diluted to 20% with deionised water. EBSD maps were acquired using a Thermo Fisher Scientific™ Quanta 250 field emission gun scanning electron microscope (FEG-SEM), with an Oxford Instruments™

Nordlys EBSD detector and the Oxford Instruments™ AztecHKL 4.1 software. This data was captured to demonstrate the qualitative output capability from the methodology and visualise the microstructural changes in the C101 material. An area of 730.4 μm × 501.6 μm with a step size of 0.8 μm was scanned per sample at location within the cogged zone. In this low magnification map example, 88% of the points were successfully indexed.

The captured EBSD data was analysed using the MTEX Toolbox [20] developed in the MATLAB® software package. The analyses showed that high angle grain boundaries (HAGBs) were predominantly observed throughout, the settings for these MTEX calculations were as follows: low angle grain boundaries (LAGBs) were defined as those with misorientations between 3° and 5°, and medium angle grain boundaries (MAGBs) were defined as boundaries with misorientation angles between 5° and 10°. HAGBs were defined according to a misorientation angle of at least 10°, and twin boundaries were defined as those with a 60°<111> misorientation, allowing an 8.66° tolerance, following the Brandon criterion [21].

Additionally, Vickers microhardness indentation maps and series measurements were captured using a DuraScan® 70 G5 hardness tester with a load of 1 kg (HV1) for a dwell time of 10s under the Vickers BS EN ISO 6507 [22] standard for all samples. These hardness maps were overlaid on the light micrograph images to compare grain structure against hardness. Indentations were made every 1.7 mm for maps and 0.7 mm for line series measurements.

4. Results

4.1. *Miniaturised open-die forging*

Equipment capability was initially tested at room temperature, starting with the benchmark, specimen SP1. Specimen SP1 was cold-worked with 5% incremental deformation (*i.e.*, reduction of cross-sectional height) in radial direction on both 0° and 90° axes. Between each of these pairs of bites the sample was removed from the holder and measured using electronic calipers, across 3 points of the cogged area and averaged. The details of these measurements are provided in Table 3, N.B. original specimen height measured as 11.59 mm.

Benchmark testing halted after the first bite at 30% as the sample sheared. Understanding of the apparatus operation, material behaviour at room temperature, expected load figures, and tooling capabilities was captured from this first test. Fig. 3(b) shows specimen SP1 after cold cogging and Fig. 4(a) shows the light microscopy appearance of the longitudinal cross-section of specimen SP1. In Fig. 4(a) it can be seen that there are visible plastic flow lines towards the edge of the transition zone, and throughout the centre of the cogged zone. Table 4 details the specimen results for the C101 copper alloy dataset, comparing target, measured, and calculated height and area reductions respectively.

Deformation resulted from all cogging trials followed a similar overall trend, with the first bite achieving a higher load than the respective second bite on the perpendicular axis. This can be seen from the load graph data of specimen SP6 in Fig. 7(a), N.B. load cell drift is observed over the course of the cogging trial. The post-analysis load graph output from DEFORM™ FE modelling of the material is provided in Fig. 7(b). It is observed that the test time for the FE predicted load graph seen in Fig. 7(b) is much shorter, as well as a more uniform increase in load for each set of bite targets. From Fig. 7(c) it is observed the model over-predicts the first bite by a significant margin (above 50%) and continues to generally over-predict the subsequent bites in

Table 3 – Per-bite target and measured cross-sectional deformation levels for Specimen SP1, deformed at ambient temperature, used as a benchmark for subsequent tests. All measurements made with electronic vernier callipers.

Target Cross-sectional Height (mm)	Measured Cross-sectional Height (mm)	Cross-sectional Height Deviation (mm)	Target Cross-sectional Height Reduction (%)	Input Cross-sectional Height Reduction (%)	Measured Cross-sectional Height Reduction (%)
11.0	11.3 ± 0.2	0.3	5	6	2.2
10.4	10.9 ± 0.2	0.5	10	12	6.3
9.9	10.4 ± 0.2	0.5	15	19	10.5
9.3	10.1 ± 0.2	0.8	20	28	13.2
8.7	9.5 ± 0.2	0.8	25	38	18.4
8.1	7.5 ± 0.2	−0.6	30	47	35.0

Table 4 – Results of geometric assessments for all C101 copper alloy specimens cogged at ambient and elevated temperatures, comparing the target cross-section height reduction, lab measured cross-section height reduction measured with vernier callipers, and the maximum and average cross-section height reductions calculated using sectioned areas from the stub and cogged zones of the 3D GOM scans. Also detailing the geometry, total number of bites, and calculated elongation percentage.

Specimen No.	SP1	SP2	SP3	SP4	SP5	SP6	SP7	SP8
Target Cross-section Reduction (%)	30(Benchmark)	5	10	15	15	30	40	10
Measured Cross-section Reduction (%)	35.0 ± 0.2	4.7 ± 0.2	10.0 ± 0.2	13.1 ± 0.2	9.7 ± 0.2	32.6 ± 0.2	41.0 ± 0.2	8.1 ± 0.2
Avg. Area Reduction (%)	29.1	0.4	4.0	8.9	4.8	46.5	52.5	13.1
Max. Area Reduction (%)	43.2 ± 1.0	7.7 ± 1.0	12.7 ± 1.0	21.8 ± 1.0	14.0 ± 1.0	54.7 ± 1.0	69.9 ± 1.0	24.0 ± 1.0
Geometry	Square	Square	Square	Square	Square	Square	Square (2 Passes)	Octagonal
Total No. of Bites	12	2	4	6	6	12	16	8
Elongation (%)	28.4	0.6	2.6	3.5	2.1	23.2	54.9	9.1
Temperature (°C)	20	20	20	20	600	600	600	600

decreasing amounts until the last bite at 30% is under-predicted by 11.3%.

4.2. *Microstructure and FEM*

Comparative GOM 3D scan results for each of the C101 specimens can be seen in Fig. 8. These scans show the final billet geometries, which are representative of billet geometries seen in industrial processes [23]. Specimen SP1 is in exception to the expected geometry, as it was the first cold-worked benchmark obtained using the designed experimental apparatus and due to this was repeatedly removed and replaced in the machine for calliper measurements. Fig. 3(a) and (b) show the specimen geometries before and after being cogged, this geometry was the result of a load-frame auto-stop after detecting shear in the sample.

Specimen SP6, shown after cogging in Fig. 3(c), is a clear example of the equipment achieving noticeable grain refinement, visible in Fig. 4(b). 94.59% reduction in grain size between the stub and cogged zones was measured using the mean linear intercept method in ImageJ. The largest grains ($\approx$25 mm^2) in the stub zone can be seen to transition quickly to a refined equiaxed structure in the cogged zone where the average grain size is ~5000 μm^2. Fig. 9(a) shows the strain distribution relative to 45% area reduction, representative of specimen SP6 after deformation, whereas Fig. 9(b) shows the relative strain distributions through each consecutive series of compressive bites. The FE results presented in 9(b) clearly shows the increase in strain imposed with % reduction. The locations close to the sharp corners at front end of the sample and close to coupling (non-deformed section) experience higher strain values. This could be due to influence of tensile stresses building up with the increase in % reduction.

Fig. 5(b) shows the obtained light micrograph of the specimen after cogging (showing evidence of grain refinement, and a barreling effect) with an overlaid Vickers microhardness map, showing an increase in hardness in the cogged zone. The FE predicted strain distribution (*i.e.*, deformed to the same strain level as the cogging trials), is presented in Fig. 5(c) which corroborates the barreling effect seen in the specimen. This allows correlation of the strain distribution to the observed grain structure refinement, demonstrating the potential predictive capability for microstructures that could be expected after forging. Fig. 10 shows light optical microscopy appearances of the three zones: stub, transition, and cogged. The micrographs reveal the variation in grain size throughout the specimen cross-section, ranging from a coarse structure in the stub zone, capturing the transition at the edge into the refined equiaxed structure in the cogged zone where the deformation was concentrated.

Microhardness measurements reveal a noticeable increase in the Vickers hardness values for the samples that have been cold-worked between the stub and the cogged zones, *e.g.*, an increase of 147.1% for specimen SP1. The samples forged at elevated temperature similarly show an increase in hardness between the stub and cogged zones, but with a lower increase of 16% for SP6. The full list of hardness increase values from the stub zone to the cogged zone of each sample can be seen in Table 5. It is evident from the

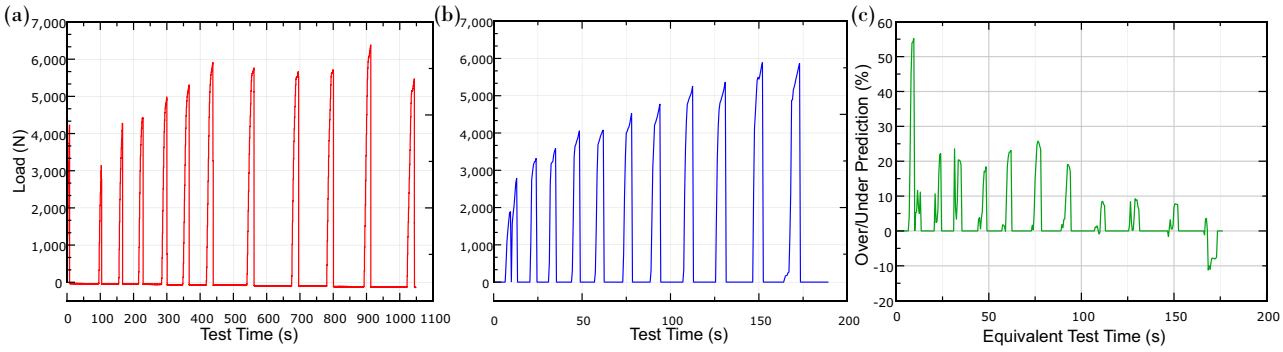

Fig. 7 – (a) Measured load (N) against test time (s) for specimen SP6 during the cogging trial. Data was taken from Zwick/Roell™ load cell during testing, recorded in Zwick™ testXpert III software, (b) The FE predicted graph for load (N) against test time (s) for C101 copper alloy to the same number of bites and, (c) Graph showing over or under prediction of the model against the captured load data as a percentage against an equivalent test time. Visualised using LabPlot by KDE®.

data in the table that the cold-worked copper has a much greater average increase in hardness by a factor of 9.2. Series measurement trend lines for SP1 and SP6, seen in Fig. 11, highlights this factor as the area reduction is approximately the same.

The captured EBSD results can be seen in Fig. 12, where Fig. 12(a) shows the band contrast output detailing the billet and the cogging directions. The IPF-CD map (out-of-page), seen in Fig. 12(c), shows a preferential alignment to the [011] direction, which correlates with one of the compression directions. Fine recrystallised grains nucleated within prior grains are also seen. The pole figures and IPF's in Fig. 12(b) reveal that there is no discernible texture after deformation. From Fig. 12(d), showing the geometrically necessary dislocations (GND) map of the area, it can be seen that the higher GND energies align with the higher levels of dislocations, in one of the compression directions, which aligns with the preferred [011] orientation seen in Fig. 12(c). GND maps were calculated using Pantleon's method [24], which uses the curvature tensors captured by EBSD, which are directly related to the dislocation density tensors according to Kröner [25].

5. Discussion

The proposed experimental set-up and pilot experiments have successfully demonstrated the capability of performing rotary open die forging or cogging at the laboratory scale, with clear evidence of microstructural control being achieved during the thermomechanical processing. However, when

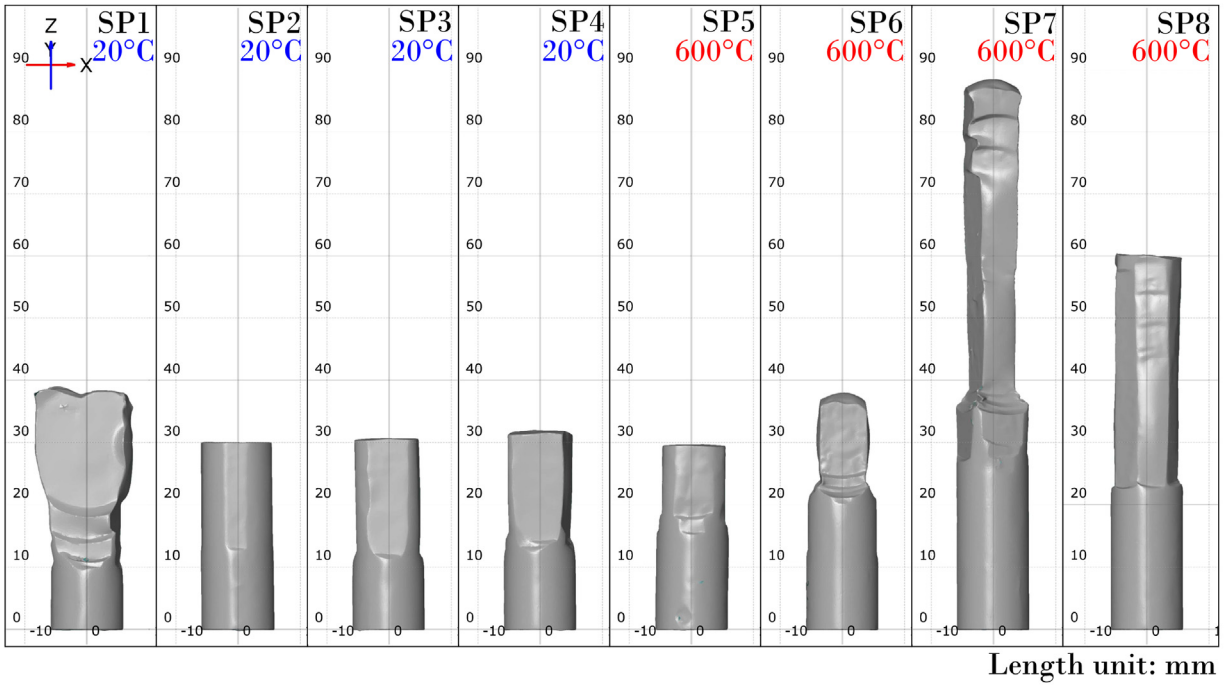

Fig. 8 – 3D GOM photogrammetry scans of copper specimen range highlighting final geometries, parts to same scale.

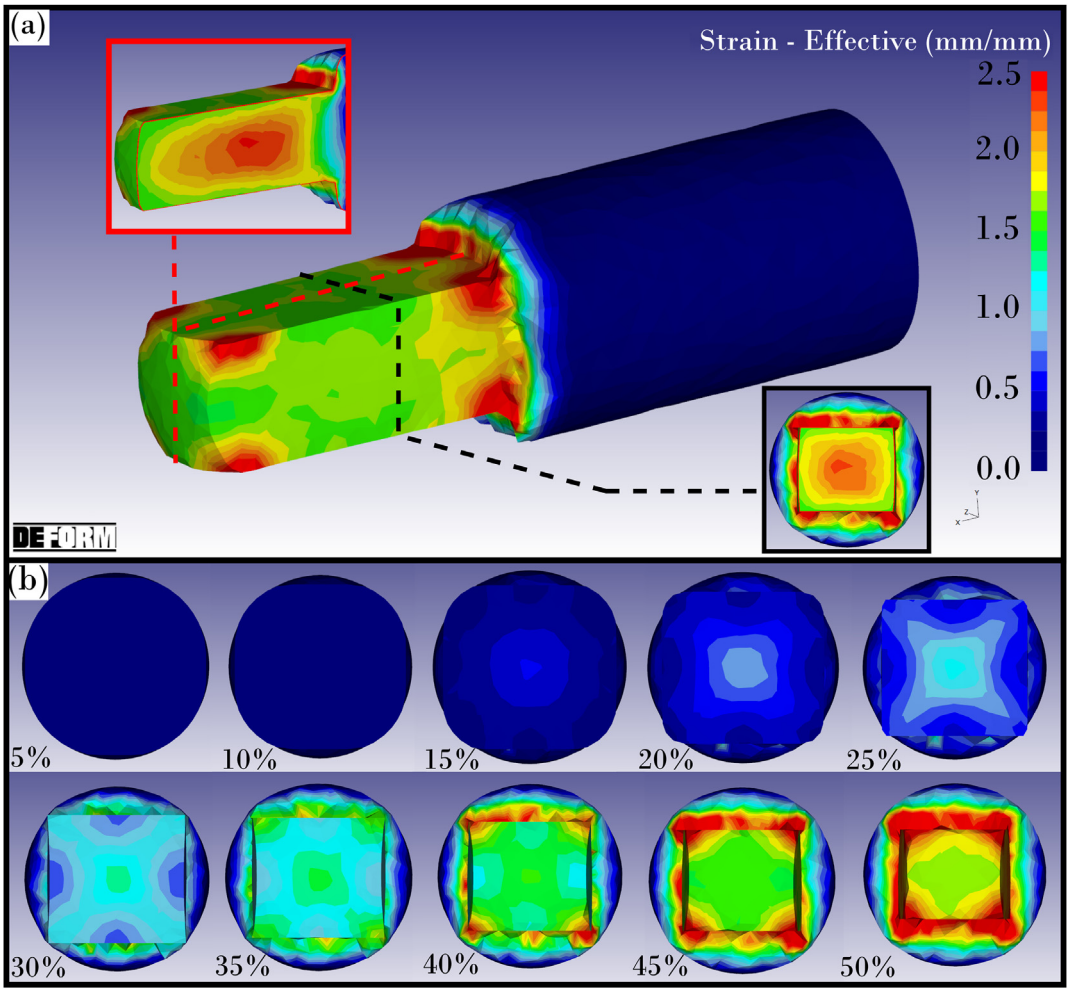

Fig. 9 – (a) The FE predicted effective strain distribution in specimen SP6 following cogging trial to 45% deformation, with the strain distributions on both the longitudinal and transverse cross sections provided, (b) The FE predicted strain distributions on the radial cross-section after each cogging pass up to 10 passes (i.e., 50% strain). The effective strain scalebar is the same for both.

considering such a reduced scale approach for studying large scale industrial manufacture, one has to be mindful of a number of limitations.

First, there are the limitations of the laboratory test environment vs. industrial facilities. For example, the present apparatus used has both the workpiece material and forging dies under isothermal conditions, whereas industrial ingot-to-billet conversion processes are non-isothermal. This means industrially, the material is losing thermal energy because it is exposed to air at the ambient temperature and because the dies are not heated to the same temperature level as the billet. This is done to prolong tool life, as die material is costly. One could assume a quasi-isothermal state due to the large thermal mass of the industrial-scale workpieces, especially within the interior. However, there is, in most cases, a discrepancy in the resulting core and surface microstructure which cannot be overlooked.

The isothermal nature of the tests also places additional strength requirements on the tooling material which is also subject to high compressive loads. Nickel-based superalloys were used in the manufacture of the dies to minimise the problem of tool wear. However, the high temperature strength of superalloys relies on the presence of a sufficient volume fraction of the γ' $L1_2$-ordered intermetallic phase which precipitates from a disordered solid solution with a face-centred cubic structure. Increasing the forging temperature closer to the γ' solvus, reduces the overall volume fraction available for precipitation strengthening, effectively weakening the die material. This, therefore, places a limit on the maximum isothermal forging temperature with the present configuration of the experimental apparatus. For example, this would present a challenge for cogging experiments on superalloys which would require temperatures in excess of 1100 °C. This could be overcome with dies made from highly sintered oxide ceramics in air, or molybdenum alloy dies under vacuum. In contrast, the cogging dies used in industry do not reach such high temperatures and hence can be manufactured from more cost-effective materials.

The present method also requires specimen alignment to be completed prior to heating, with pre-loads being introduced

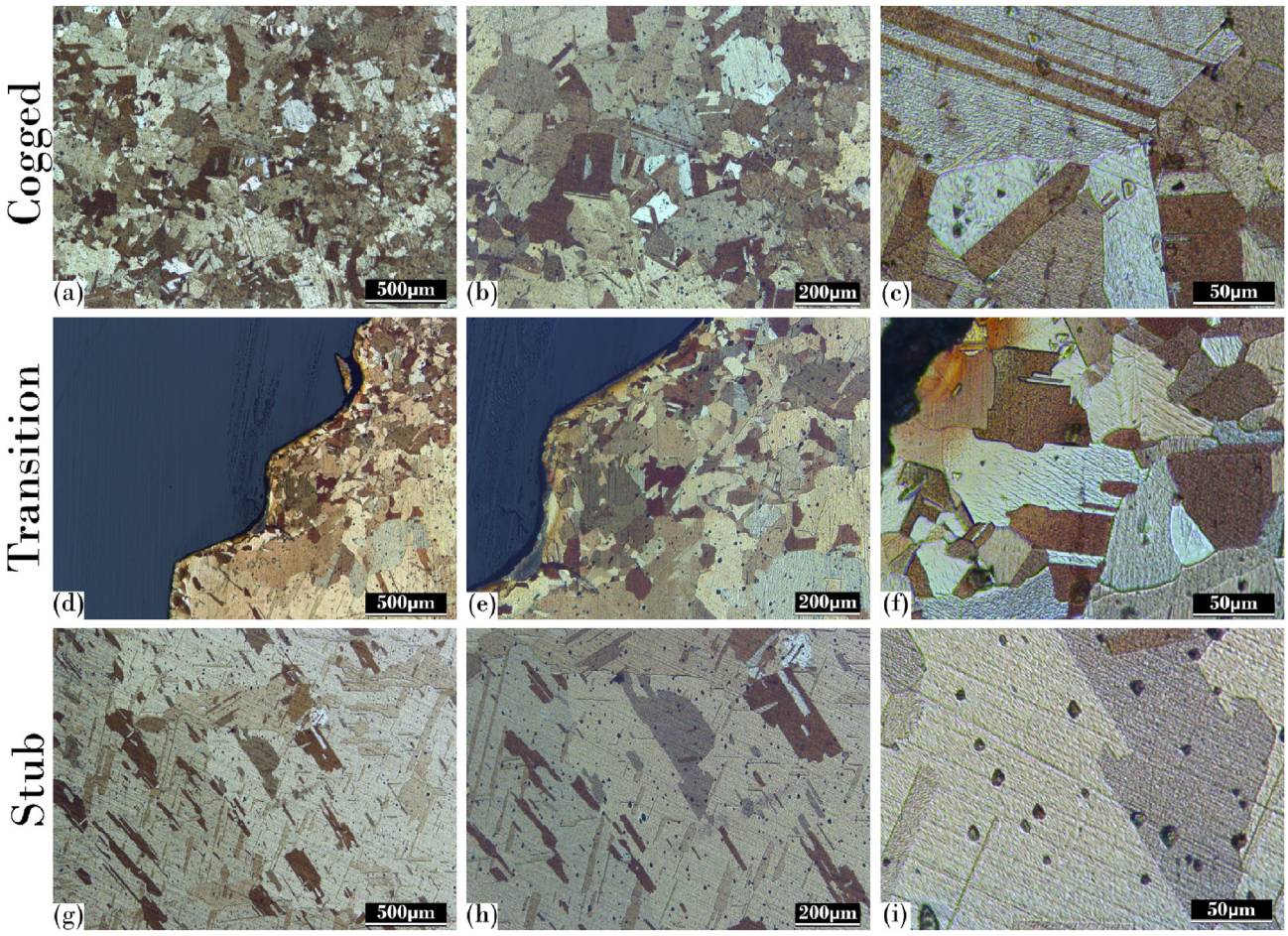

Fig. 10 – Optical micrographs taken from different zones of the cross-section of the SP6 specimen after forging at 3.5 ×, 7 ×, 35 × magnifications: (a)–(c) Cogged zone, (d)–(f) Transition zone, (g)–(i) Stub zone.

when the sample is close to forging temperature. The apparatus, in its current form, also does not allow re-coating of the dies with boron nitride lubricant. As a result, the friction coefficient increases with progressive forging bites as the initial coating (applied prior to heating) is depleted. This loss of lubricant from the surface of the dies can also lead to the sticking of the workpiece to the compression dies. While this was not found to be problematic with specimens with a round initial cross section, samples with initially rectilinear cross-sections were found to be more prone to sticking due to increased surface area contact with die surfaces. The risk of sticking was also found to increase when a higher strain/displacement per bite was used, *i.e.,* higher load, and reduced number of passes. The higher friction can also lead to more pronounced barreling of the specimen, which may subsequently complicate specimen rotation due to convex surfaces and protruding corners catching on the compression platens.

The geometry of the sample is also important to consider. Extruded cylindrical bars were used for this study, leading to increased risk of sideways slippage of the samples during initial bites. Once these first chamfers/flats were generated, the risk of slipping greatly decreased. For specimen SP8, which was an exploratory sample in octagonal cogging, it was found that due to the size effects of the sample geometry it was of even higher risk of slipping into one of the already created flat faces. Furthermore, as it was repeatedly deformed, it became apparent that this slippage increased with passes as the bite surface area was progressively decreased.

Table 5 – Vickers hardness results for C101 alloy deformed at ambient and elevated temperatures, highlighting the average hardness measured in the stub and cogged zones, and the overall percentage increase in hardness.

Specimen No.	SP1	SP2	SP3	SP4	SP5	SP6	SP7	SP8
Temperature (°C)	20	20	20	20	600	600	600	600
Avg. Hardness in Stub Zone (HV)	53.0 ± 0.5	48.1 ± 0.5	50.1 ± 0.5	54.0 ± 0.5	44.2 ± 0.5	42.9 ± 0.5	45.9 ± 0.5	46.4 ± 0.5
Avg. Hardness in Cogged Zone (HV)	131.0 ± 0.5	72.2 ± 0.5	94.4 ± 0.5	113.6 ± 0.5	48.7 ± 0.5	49.7 ± 0.5	48.4 ± 0.5	51.8 ± 0.5
Hardness Increase (%)	147.1 ± 1	50.1 ± 1	88.4 ± 1	110.4 ± 1	10.1 ± 1	16 ± 1	5.5 ± 1	11.76 ± 1

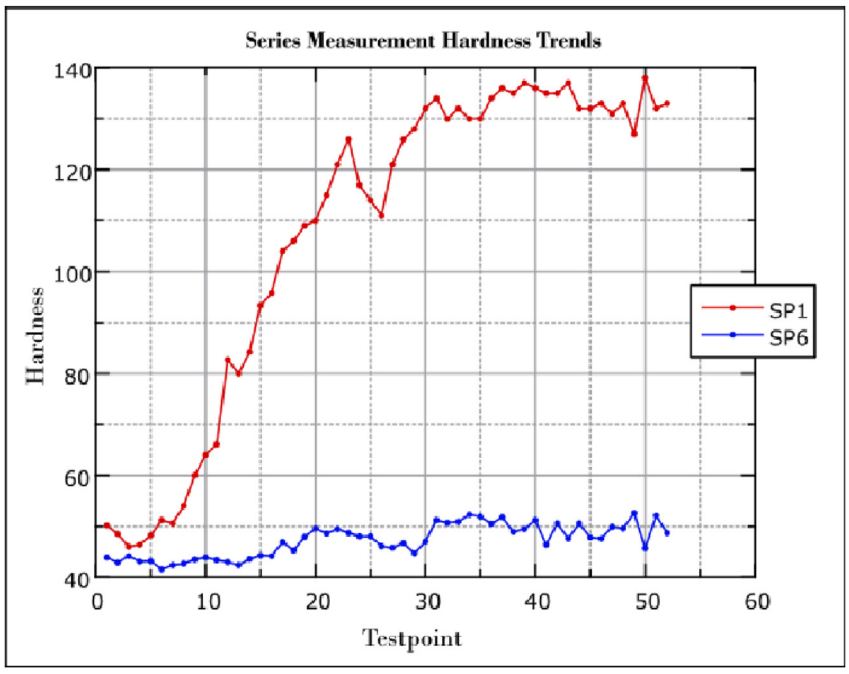

Fig. 11 – Vickers hardness trend lines for specimen SP1 (red) cogged at room temperature, and specimen SP6 (blue) cogged at 600 °C.

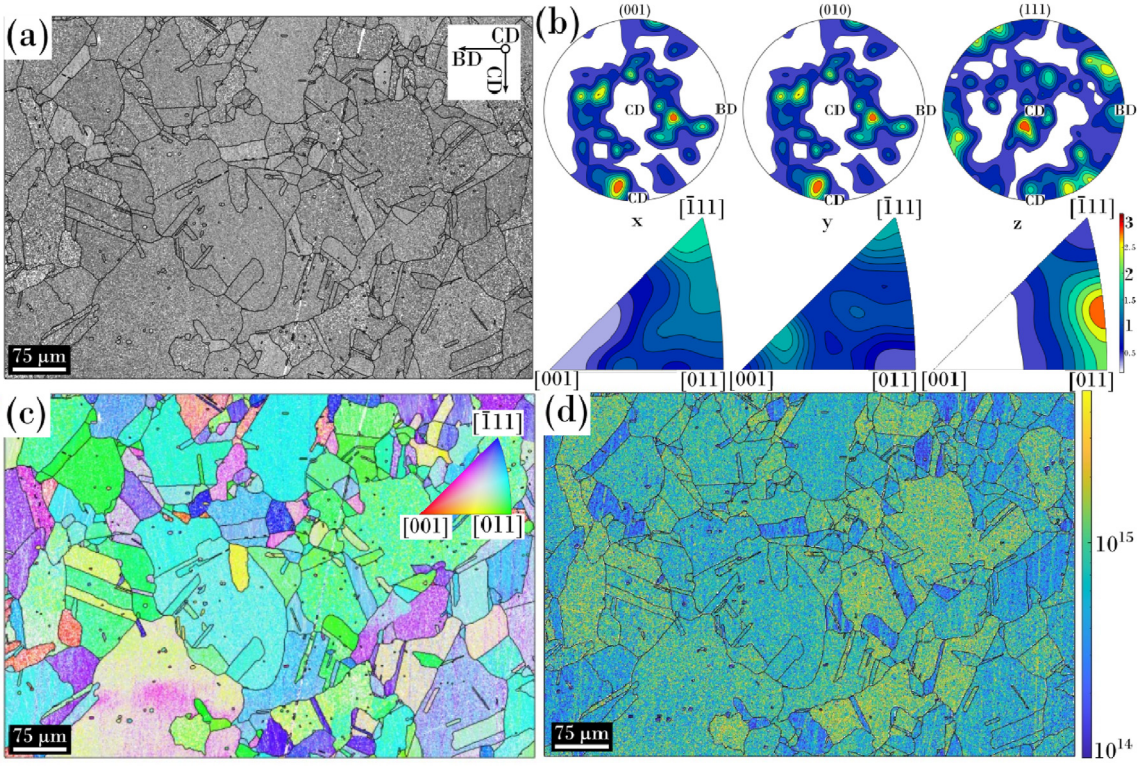

Fig. 12 – EBSD results captured from the cogged zone of specimen SP6, deformed at 600 °C to 45.6% reduction in area, equivalent to an effective strain of ε ≈ 2.5; (a) Band contrast map highlighting grain boundaries and with labelled Billet Direction (BD), and Cogging Directions (CD), (b) Pole figures and Inverse pole figure diagrams (c) IPF-CD map (out-of-page), (d) GND density distribution map, colour scale indicates log (GND density in lines/μm^2).

The compensation of tooling loss, detailed previously in Tables 3 and 4, was approximated from the benchmark sample through increased input loads to achieve strains closer to the target strain. Further exploration and consolidation of this method would benefit from further study. Despite having isothermal conditions, small fluctuations of 3–4 °C were observed when the specimen was rotated, possibly caused by small air vortices introduced by the motion and affecting thermocouple readings. Another possible cause is leakage of hot air through the extensometer slot.

Specimen alignment is also complicated by the restricted or null visibility of the specimen when a split tube furnace or EC is used for isothermal experiments. Fine adjustment of the specimen position had to be done prior to heating. Moreover, thermal expansion of the specimens, sample holder, and tooling is important to consider during the temperature ramp-up. During pre-deformation alignment, and checks between bites, a small viewing window in the EC chamber proved highly valuable. The visibility decreases with increasing test temperature (above 600 °C), as, without special modifications, tube furnaces do not provide any way of observing the furnace interior during operation.

In addition to the limitations of using laboratory equipment, some material-specific limitations need to be determined individually for the types of test being carried out. Size effects in materials, can be pronounced and very influential to the overall method and component design. Such effects can be of crucial importance when performing material studies, as phenomena that occur at large scale may not be observable at small scale and vice versa. The specimen size was chosen primarily based on the internal chamber volume of the furnace, as well as initial strength properties with respect to load frame capability. Furthermore, the die shape is important to consider. The flat circular or disc-shaped design was used firstly to replicate the flat-dies used in industry open-die forging, but also to protect laboratory equipment and tooling, as to not adversely and undesirably concentrate loading in the load frame for the first testing of this method.

With large industrial billets, strain rates are kept low due to the large masses involved and where the deformation is limited, evidence can be seen in the work of Paquette et al. [26] The nominal strain rate of $0.01s^{-1}$ ($\dot{\varepsilon}_m$) was selected to simulate the large industrial multi-tonne ingot to billet conversion, and was additionally suitable for these tests to protect the equipment and tooling rods of the load frame, as this was the first trial of the method. Typically, larger strain rates are used in closed-die forging operations. However, it is possible for higher strain rates to be explored in future iterations of testing as these first tests have validated the operation of the new equipment.

There are some established devices that are used for measuring plastic flow and can simulate thermomechanical deformation, *e.g.,* Gleeble®. However, Gleeble®'s temperature distribution control is somewhat less accurate than what this isothermal set-up can provide. It also cannot perform isothermal cogging (*i.e.,* open-die forging) and the rotational movement to the same degree of freedom and accuracy, however one similar study was completed by Bereczki et al. [27] where multi-axial forging trials were carried out on a MAXStrain system. Load frames across materials testing laboratories are also typically more common than that of a Gleeble® device, allowing for wider application of this method.

Specimen SP1 demonstrated that a greater nominal input strain or load would be required to achieve the low strain targets. This trend continued with all future cold-worked sample results, where larger inputs, or initial losses in tooling and elastic material properties require larger compensation. Where accelerated compensation is required as the strain target climbs, there is an unknown yield point in the material and tooling where the compensation values balance. This trend was also observed in samples deformed at elevated temperature, although a decrease in the overall load required was seen. A similar degree of compensation was required for the machine and tooling to achieve the required target strain.

Plastic flow lines can be seen in Fig. 4(a), which can be expected from localised plastic deformation [28]. Optically, the size of the elongated grains of the cold-worked material was found to be more difficult to determine in the areas with flow lines. This could be indicative of these areas being characterised by ultrafine nano-sized grains after dynamic loading [29–31]. At the transition zone edges, stretching effects are visible where the grains have been elongated and follow the curvature of the edge. Interestingly, longer samples (*e.g.,* SP8) with multiple passes along the main axis have shown signs of dynamic recrystallisation and grain growth in sections of earlier bites. Re-validating the potential for the studies that could be explored using this experimental method.

Material studies with the designed apparatus have already extended into trial studies with 6000 series aluminium alloy as well as commercial dual-phase titanium alloy (Ti–6Al–4V). It has also been employed in further research projects, simulating the cogging process on Ti–6Al–4V material, that can then be fed upstream into larger research-scale cogging trials on a 500-tonne press and equivalent models. Future employment of this apparatus can also be used to inform industrial scale open-die forging, in terms of assessing the key process parameters, such as strain and strain rate, required to initiate onset of recrystallisation during ingot-to-billet conversion, and thus save costs in material, energy, and time of performing minimum number of tests. These studies provide proof that a wide range of materials can be tested using the presented experimental method, including commercial alloys which are of high research interest. Specifically, the capability of hot forging titanium alloys was a requirement that guided a number of design decisions with regard to the load frame capacity, specimen size with respect to available furnace volume, as well as the choice and geometry of tooling materials.

5.1. *Future design considerations*

Greater investment in robust components and more focused adaptation of pre-existing equipment fixtures and features, could further improve the efficacy and robustness of the apparatus design.

Firstly, designing for portability was one major benefit of this method as it could be used with any load frame system using the current tripod-mounted configuration. However,

some load frames provide existing external mounts, allowing for rig mounting to the pre-existing extensiveness fixtures, *e.g.,* mounting arms available on some Zwick/Roell™ load frames, typically used for extensometers. This would allow for more consistent specimen alignment and reduce the alignment time, allowing a faster specimen turnover. In addition, increasing the holding torque on the sample via the use of more powerful stepper motors (*e.g.,* NEMA23) would further increase the resistance to slippage. The addition of a third motor system would aid to compensate for the vertical displacement of the specimen during compression, rather than relying on deflection of the long manipulator rod to accommodate this displacement. It would also help fine position adjustments.

Another consideration would be the "flying-blind" nature of the method at higher forging temperatures (>600 °C) using tube furnaces. A small form factor optical fibre-optic camera solution could provide an invaluable additional degree of workpiece position control during operation. It would allow the state of the specimen after each bite to be evaluated and adjustments to be made accordingly. Alongside this system, an in-situ lubrication injection system could prove highly beneficial, if not a necessity, when studying greater levels of strain during hot forging at temperatures exceeding 900 °C. Exploration of the use of graphite films may also provide useful as future work. As the isothermal conditions and repeat passes remove lubricant from the sample, the risk of sticking increases the longer the test runs. In-situ lubrication is used in many larger scale research and industry to not only ensure die/workpiece separation and lower friction, but preferably to also act as a thermal insulator.

Routine programs can be created alongside the load frame control software (*e.g.,* Zwick™ textXpert III) to fully automate each process. Addition of the BNC connections was primarily done to automate this process, however, was never tested due to external circumstances and early-stage nature of this work. This change could increase positional accuracy, and throughput of testing.

Die design is also an avenue of research that could be explored using this new equipment, as flat rectangular dies could be used where the appropriate consideration and set up is considered for the load frame equipment and tooling accessories. These die designs could lead to decreased sticking, with reduced surface area of the sample being compressed during each bite and be more representative of industrial die tooling. Parameter testing for radial forging, where V-shaped dies are used, may also be considered for this apparatus in future experimentation. Altering temperature, strain, and material was tested, however future work could also consider the impact of increasing strain rate on materials testing with this method.

A final consideration is in the design of the coupling tooling. Currently, grub screws are used to hold the sample and manipulator rod in place. This works well for the manipulator rod, however, as specimens need to be repeatedly inserted and removed from this coupling, this design may not be optimal for high temperature applications due to the reduced longevity of the grub screws. The thermal expansion and oxidation that may occur, can lead to seizure of the workpiece inside the barrel of the specimen holder. Inclusion of a capped pin/pin system, or lock-and-key design, could eliminate this issue, at the expense of more complex sample and holder machining that would be required.

6. Conclusion

This study has investigated the feasibility of laboratory-scale testing and investigation of cogging processes used for ingot-to-billet conversion in high-value engineering components manufacture. It has been successfully demonstrated that a comparatively inexpensive apparatus can be constructed using readily available mechatronics components with a very limited number of custom-made high temperature parts and used for this purpose with a conventional uni-axial load frame typically available in most materials testing laboratories.

The pilot high-temperature cogging trials carried out on a C101 copper alloy have been used to develop the foundation for a testing methodology and have shown the ability of the approach to achieve significant grain refinement via recrystallisation and recovery. An average grain size reduction, refinement from 25 mm^2 down to 5000 μm^2, has been demonstrated in a specimen deformed to 46.5% of its original cross-sectional area. In conjunction with modern characterisation techniques, the proposed apparatus and methodology could provide a cost-effective way of investigating the phenomenology of microstructural evolution during the complex multi-step forging processes, such as cogging and upsetting operations.

The new insights gained from miniaturised testing may help inform more costly intermediate-scale testing and provide data for development of new plasticity models, which could be used to develop digital twins for the next-generation of digital metallurgical manufacturing. While the presented pilot investigation has its limitations, notably the extent of applicability to industry-scale, there is ample opportunity for further refinement of the methodology and its use in the identification of possible size-effects, so this investigation aspires to provide a platform for further scientific research and discussion.

Data availability

The raw/processed data required to reproduce these findings cannot be shared at this time as the data also forms part of an ongoing study.

Credit authorship contribution statement

David Connolly: Methodology, Validation, Formal analysis, Investigation, Data curation, Writing – original draft, Visualisation.

G.Sivaswamy: Supervision, Writing - review & editing **S. Rahimi:** Conceptualisation, Supervision, Writing - review & editing.

V.Vorontsov: Conceptualisation, Supervision, Project administration, Writing - review & editing.

Declaration of Competing Interest

The authors declare that they have no known competing financial interests or personal relationships that could have appeared to influence the work reported in this paper.

Acknowledgements

The authors would like to acknowledge the support provided by the Advanced Forming Research Centre (*AFRC*), University of Strathclyde, which receives partial funding from the UK's High Value Manufacturing CATAPULT. VAV would also like to acknowledge funding support from the University of Strathclyde under the Chancellor's Fellowship scheme. DJC and VAV also thank Dr. Vivian Tong, Mr. Tony Fry, and Dr. Ken Mingard (National Physical Laboratory) for valuable training and consultation, and Sebastien Nouveau (Aubert & Duval) for constructive discussion that led to this study. DJC would also like to thank Mr. Michael McCracken for his assistance during initial trials.

Appendix A. Supplementary data

Supplementary data to this article can be found online at https://doi.org/10.1016/j.jmrt.2023.08.073.

REFERENCES

[1] Yeom JT, Lee CS, Kim JH, Park N-K. Mater Sci Eng 2007;A 449–451:722–6. https://doi.org/10.1016/j.msea.2006.02.415. proceedings of the 12th International Conference on Rapidly Quenched & Metastable Materials.

[2] Coyne-Grell A, Blaizot J, Rahimi S, Violatis I, Nouveau S, Dumont C, et al. J Alloys Compd 2022;916:165465. https://doi.org/10.1016/j.jallcom.2022.165465.

[3] Coyne-Grell A, Blaizot J, Rahimi S, Violatos I, Nouveau S, Dumont C, et al. Metallurgical and materials transactions A: physical metallurgy and materials science. J Alloys Compd 2023;54(5):2022–36. https://doi.org/10.1007/s11661-022-06878-w. cited by: 0; All Open Access, Green Open Access, Hybrid Gold Open Access.

[4] Kukuryk M. J Appl Comput Mech 2018;17:45–52. https://doi.org/10.17512/jamcm.2018.3.04.

[5] Cho JR, Park CY, Yang DY. Proceedings of the institution of mechanical engineers. Pa Birds: Journal of Engineering Manufacture 1992;206~(4):277–86. https://doi.org/10.1243/PIME_PROC_1992_206_084_02. *arXiv*.

[6] Dong J, Li L, Li H, Zhang M, Yao Z. Acta Metall Sin 2015;51~(10):1207. https://doi.org/10.11900/0412.1961.2015.00419.

[7] Pérez M, Dumont C, Nodin O, Nouveau S. Mater Char 2018;146:169–81. https://doi.org/10.1016/j.matchar.2018.10.003.

[8] Souza P~M, Sivaswamy G, Bradley L, Barrow A, Rahimi S. J Mater Sci 2022;57(44):20794–814. https://doi.org/10.1007/s10853-022-07906-1.

[9] Souza P~M, Sivaswamy G, Hall L, Rahimi S. Int J Mech Sci 2022;216:106975. https://doi.org/10.1016/j.ijmecsci.2021.106975.

[10] ASTM. Standard practice for compression tests of metallic materials at elevated temperatures with conventional or rapid heating rates and strain rates. Int J Mech Sci 2018. https://doi.org/10.1520/E0209-18.

[11] M. Ward, Ironmak Steelmak 42~(4) (2015) 252–258. *arXiv*:https://doi.org/10.1179/0301923314Z.000000000347.

[12] S. Rahimi, I. Violatos, B. Wynne, M. Jackson, Mater World 30~(6) (2022) 38–41. https://www.iom3.org/resource/digital-twins-for-high-value-components.html.

[13] Blackwell PL. International Conference on New Forming Technology. CHN; 2015. https://doi.org/10.1051/matecconf/20152101004.

[14] Huang SH, Chai SX, Xia XS, Chen Q, Shu DY. Strength Mater 2016;48~(1):98–106. https://doi.org/10.1007/s11223-016-9743-6.

[15] Taylor GI, Quinney H. The latent energy remaining in a metal after cold working. Proceedings of the Royal Society of London. Series A Containing Papers of a Mathematical and Physical Character 1934;143~(849):307–26. https://doi.org/10.1098/rspa.1934.0004.

[16] Kulakov M, Rahimi S, Semiatin SL. Metall Mater Trans 2022;53~(2):407–19. https://doi.org/10.1007/s11661-021-06493-1.

[17] Rittel D, Zhang LH, Osovski S. The dependence of the Taylor-Quinney coefficient on the dynamic loading mode. J Mech Phys Solid 2017;107:96–114. https://doi.org/10.1016/j.jmps.2017.06.016.

[18] Charles HMM, Lieou KC, Bronkhorst CA. Int J Plast 2019;119:171–87. https://doi.org/10.1016/j.ijplas.2019.03.005.

[19] Soares G~C, Hokka M. Int J Impact Eng 2021;156:103940. https://doi.org/10.1016/j.ijimpeng.2021.103940.

[20] Bachmann F, Hielscher R, Schaeben H. Ultramicroscopy 2011;111~(12):1720–33. https://doi.org/10.1016/j.ultramic.2011.08.002.

[21] Brandon DG. The structure of high-angle grain boundaries. Acta Metall 1966;14(11):1479–84. https://doi.org/10.1016/0001-6160(66)90168-4.

[22] I. O. for Standardization (ISO), Metallic materials: Vickers hardness test, ISO 6507-1:2018 (2018). *doi*:https://doi.org/10.3403/BSENISO6507.

[23] Open-Die Forging. In: Semiatin L, editor. Metalworking: Bulk Forming, ASM Handbook, 14A. ASM International; 2005. p. 99–110. https://doi.org/10.31399/asm.hb.v14a.a0003978.

[24] Pantleon W. Scripta Mater 2008;58~(11):994–7. https://doi.org/10.1016/j.scriptamat.2008.01.050.

[25] Kroner E. Dislocations and continuum mechanics. Appl Mech Rev 1962;15~(8):599–606.

[26] Paquette A, Rahimi S, Violatos I, Langlois L, Dumont C, Blaizot J, et al. R.Bigot 24th ESAFORM conference on material forming. ESAFORM 2021. https://doi.org/10.25518/esaform21.929.

[27] Bereczki P, Fekete B, Szombathelyi V, Misjak F. Mater Perform Charact 2015. https://doi.org/10.1520/MPC20150006.

[28] Wang R, Zhang H, Tang L, Shao J, Xiao Z, Chen Z, et al. Mater Sci Eng, A 2019;754:330–8. https://doi.org/10.1016/j.msea.2019.03.067.

[29] Mishra A, Martin M, Thadhani N~N, Kad BK, Kenik EA, Meyers MA. Acta Mater 2008;56~(12):2770–83. https://doi.org/10.1016/j.actamat.2008.02.023.

[30] Murr LE, Ramirez AC, Gaytan SM, Lopez MI, Martinez EY, Hernandez DH, et al. Mater Sci Eng, A 2009;516~(1–2):205–16. https://doi.org/10.1016/j.msea.2009.03.051.

[31] Yang D, An Y, Cizek P, Hodgson P. Development of adiabatic shear band in cold-rolled titanium. Mater Sci Eng, A 2011;528~(12):3990–7. https://doi.org/10.1016/j.msea.2011.01.10.